

Single-Wall-Carbon-Nanotube–VSe₂ Nanohybrid for Ultrafast Visible-To-Near-Infrared Third-Order Nonlinear Optical Limiters

Vinod Kumar¹, Dipendranath Mandal¹, K. A. Sree Raj,² Brahmananda Chakraborty,^{3,4} Amit Agarwal,⁵ Chandra S. Rout¹,² and K.V. Adarsh^{1*}

¹Department of Physics, Indian Institute of Science Education and Research Bhopal, Bhopal 462066, India

²Centre for Nano and Material Science, Jain University Jain Global Campus, Jakkasandra, Ramanagaram, Bangalore 562112, India

³High Pressure and Synchrotron Radiation Physics Division, Bhabha Atomic Research Centre, Trombay, Mumbai 400085, India

⁴Homi Bhabha National Institute, Mumbai 400085, India

⁵Department of Physics, Indian Institute of Technology, Kanpur 208016, India

(Received 19 July 2022; revised 31 January 2023; accepted 21 March 2023; published 26 April 2023)

An ideal third-order nonlinear optical material, which can efficiently absorb and refract light over a broad spectral range, is of both fundamental and technological significance as it enables many helpful functionalities in photonics. However, the optical nonlinearities are rather weak due to their perturbative nature and are limited to electronic resonances, thus restricting the response to a narrow spectral range. A charge-coupled donor-acceptor material pair can enhance the nonlinear optical response and circumvent the narrow spectral range limitation. However, such studies on potential material pairs remain largely unexplored. Here, we report the experimental observation of ultrafast third-order nonlinear optical response spanning the entire visible-to-near-infrared (400–900 nm) region in single-wall-carbon-nanotube (SWCNT)–VSe₂ nanohybrid in the strong coupling regime, enabled by efficient charge transfer. Compared to control systems, the measured nonlinear absorption and refraction of the nanohybrid show unprecedented or many-fold enhancements. Further, our density-functional theory and Bader-charge analysis show the strong electronic coupling of the nanohybrid in which the electrons are transferred from VSe₂ to SWCNT, verified by steady-state and time-resolved photoluminescence measurements. The physics of the ultrafast nonlinear optical response is well captured by our five-level rate-equation model both qualitatively and quantitatively. Using the nanohybrid, we design a liquid cell-based optical limiter with an order of magnitude better device performance parameters, such as the optical limiting onset (2.5–8.0 mJ cm⁻²) and the differential transmittance (0.42–0.62), compared to several other benchmark optical limiters in the femtosecond regime.

DOI: 10.1103/PhysRevApplied.19.044081

I. INTRODUCTION

A broad and vigorous nonlinear absorption and refraction of photons by materials is a long-standing goal of both fundamental and technological interest since they enable many helpful functionalities in photonics [1,2]. For example, as an ultrafast optical switch in quantum information processing [3,4] and communication [5], optical limiters for protecting the eyes, detectors and optical components [6,7], pulse compressors for generating ultrashort laser, and passive mode-locking saturable absorber [8–10]. Examples of third-order nonlinear optical response are intensity-dependent refractive-index change, two-photon absorption (TPA), and excited-state absorption

(ESA). However, the third-order nonlinear optical response of all materials, in general, is rather weak as it originates from the higher-order nonlinear terms and displays only a narrow spectral range in the vicinity of the electronic resonance [11]. A large magnitude of Kerr nonlinearity expressed as the real and imaginary part is particularly useful to minimize the power requirements and size of the photonic devices.

Typical examples of materials that show third-order nonlinear optical response are amorphous chalcogenide glasses [12,13], graphene oxide (GO) [14], transition-metal dichalcogenides (TMDs) [15,16], single- and multiwall carbon nanotube [17,18], porphyrin [19], plasmonic materials [20], quantum dots [21], and optical fibers [22]. Unfortunately, these materials show optical nonlinearity over a narrow spectral range in the vicinity of the

*adarsh@iiserb.ac.in

electronic resonance. Therefore, materials showing strong third-order nonlinear absorptive and refractive responses over a broad spectral range are completely missing and yet to be explored. One promising method to achieve large ultrafast Kerr nonlinearities over a broad spectral range is by the charge transfer of a donor-acceptor pair at the nanoscale interface. For example, enhanced nonlinear absorption was achieved in donor-acceptor composite such as MoSe₂/GO [23], Au-NP/GO (reduced GO) [7], Ag-NP/GO [24], MoS₂/graphene [25], Ag/Fe₃O₄ [26], MoTe₂/MoS₂ hybrid film [27] and organic-inorganic halide perovskites [28], etc. However, most of these composites show enhanced nonlinear optical response only in a narrow bandwidth in the nanosecond pulse regime due to the slow charge transfer. So, finding suitable donor-acceptor nanomaterials operating over a broad spectral range at an ultrafast timescale is a real challenge.

To address this problem, we select a nanohybrid of VSe₂ an emerging TMD in recent times [29–31] and a single-wall carbon nanotube (SWCNT) [32,33] as the donor-accepter pair. Our motivation to stem out for selecting these materials is (1) VSe₂ is a two-dimensional (2D) material with high carrier mobility [34], exceptional intercalation activity [35], unique charge-density wave [36] and other excellent characteristics to become a good candidate for donor material and (2) one-dimensional (1D) SWCNTs made of one-atom-thick graphene sheet showing van Hove singularities in their density of states is an excellent candidate for acceptor material [37]. Combining these van Hove singularities in the electronic density of states of SWCNT and the broad visible-to-near-infrared absorption spectrum of VSe₂ can, in principle, provide large Kerr nonlinearity over a broad spectral range. However, studies on semiconducting MoS₂ and multiwall carbon nanotube (no van Hove singularity) hybrids show enhanced Kerr nonlinearity, but this is limited only to the wavelengths of electronic resonance [38]. Here, we demonstrate an unprecedented or many-fold enhancement in the magnitude of the real and imaginary part of the third-order nonlinear optical response of the nanohybrid over the entire visible-to-near-infrared (400–900 nm) region compared to control systems. The observed hallmark result is attributed to the charge transfer, and our first-principles-based calculations using the density-functional theory and Bader-charge analysis show electrons are transferred from VSe₂ to SWCNT. The charge transfer is further experimentally supported by steady-state and time-resolved PL measurements. Our five-level rate-equation model captures the broad enhancement in the magnitude of the third-order nonlinear optical response in the nanohybrid. The quality of the nonlinear data recorded from repeat measurements at intensities as high as 167 GW cm⁻² symbolizes their considerably high optical damage thresholds in a distilled water dispersion, ensuring their robustness in practical applications. By exploiting the broad nonlinear optical response of the

nanohybrid, we fabricate a high-performance liquid cell-based ultrafast optical limiter with key device parameters, such as the optical limiting onset of 2.5–8.0 mJ cm⁻² along with low limiting differential transmittance 0.42–0.62 over the entire visible-to-near-infrared region. These device performance parameters are much better than that found in other benchmark optical limiters in the femtosecond regime.

II. SAMPLE PREPARATION AND PHYSICAL CHARACTERIZATION

A strongly coupled SWCNT–VSe₂ nanohybrid is prepared by the one-pot synthesis method shown in Fig. 1(a), and the details are presented in Sec. S1 within the Supplemental Material [39]. The scanning electron microscope (SEM) image in Fig. 1(b) shows the hexagonal sheet-like structure of control VSe₂, which is similar to an earlier report [40]. The SEM image of the nanohybrid clearly illustrates the threadlike structure of SWCNT that interconnects the VSe₂ hexagons, indicating their strong coupling. The powder x-ray diffraction (PXRD) pattern of the nanohybrid and controls are shown in Fig. S1 within the Supplemental Material [39]. The PXRD pattern of the nanohybrid is visibly similar to that of VSe₂, which completely matches with the JCPDS card no. 89-1641. The diffraction peaks for the SWCNT in the PXRD are shadowed by contributions from the intense peaks of the highly crystalline VSe₂. The Raman spectra of the nanohybrid and controls are recorded with a Horiba LabRAM high-resolution (approximately 1 cm⁻¹) spectrometer using an excitation of 632.8 nm from a He-Ne laser. Figure 2(a) (upper panel) displays the Raman spectrum of SWCNT, which shows characteristics *D* (disordered carbons, edges, and defects) and *G* (phonons of the *sp*² C atom of the graphite lattice) modes at 1308 and 1526 cm⁻¹, respectively [41]. The *G* mode of SWCNT is blueshifted compared to the graphite mode (1580 cm⁻¹) [42]. The peak intensity ratio (*I_G*/*I_D*) of the *G* and *D* modes give a rough measure of the structural quality of SWCNT, and the value of 10.4 in our case indicates a high-quality SWCNT sample [43]. Apart from the two prominent *D* and *G* modes, we could also observe the radial breathing mode (RBM), weak RBM+*G* mode, and *G'* mode at 188, 1722, and 2604 cm⁻¹, respectively. The frequency of the RBM mode is given by [(234/*d*) + 10] [44,45], and it can be used to estimate the tube diameter (*d* in nm). We find that the estimated diameter of our SWCNT is in the range of approximately 0.56–1.5 nm. Figure 2(a) (middle panel) shows the Raman spectrum of the control VSe₂ [46,47] having characteristic peaks at 118, 138, 257, 698, and 996 cm⁻¹. Detailed Raman analysis can be seen in Sec. S3 within the Supplemental Material [39]. The Raman spectrum of the nanohybrid is shown in Fig. 2(a) (lower panel), and it can be described as a combination of *D* and *G* modes

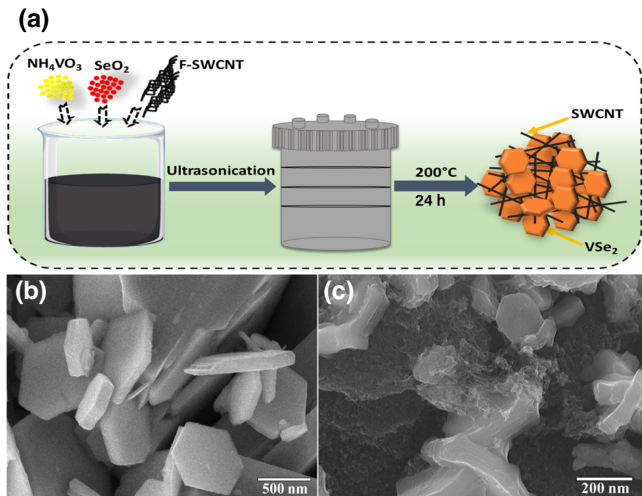


FIG. 1. (a) Schematic showing the details of sample preparation. SEM images of (b) VSe₂ and (c) SWCNT–VSe₂ nanohybrid.

of SWCNT and A_{1g} and E_g modes of VSe₂. Strikingly, we find that in the nanohybrid, the A_{1g} mode is redshifted, whereas the D and G modes are blueshifted compared to the controls. This indicates a strong electronic coupling of VSe₂ with SWCNT [48].

Having demonstrated the strong electronic coupling in the nanohybrid, we present the optical absorption spectrum in Fig. 2(b). The single absorption peak approximately 200 nm observed for SWCNT is attributed to the plasmon resonances of free π electrons [49]. The sharpness of the peak indicates the uniformity in tube length and diameter

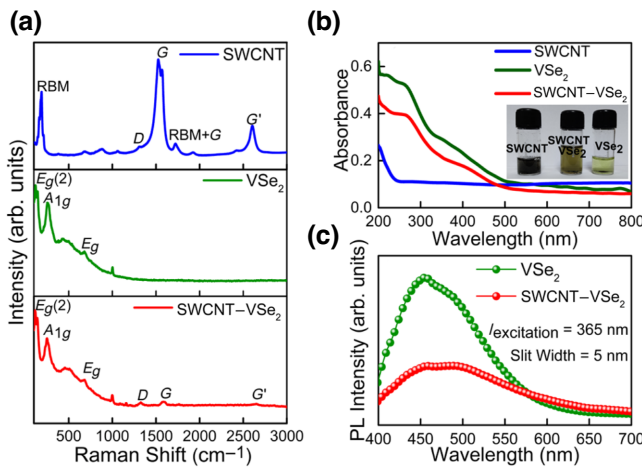


FIG. 2. Raman spectrum of (a) SWCNT (top), VSe₂ (middle), and SWCNT–VSe₂ (bottom). (b) Optical absorption spectra of SWCNT, VSe₂, and SWCNT–VSe₂ nanohybrid. (c) PL spectra of VSe₂ and SWCNT–VSe₂ nanohybrid. The PL intensity is drastically reduced and redshifted by 10 nm in the nanohybrid compared to VSe₂, indicating an efficient charge transfer.

of SWCNT. VSe₂ shows an absorption onset at 500 nm. This is in stark contrast to bulk VSe₂, which is a semimetal with no characteristic absorption feature in the UV-visible region. However, in the nanostructure, it behaves more like a semiconductor. The optical absorption spectrum of the nanohybrid can be interpreted as a superposition of signals from each control, however, the overall signal is redshifted compared to VSe₂, indicating charge transfer from VSe₂ to SWCNT.

To probe the charge-transfer mechanism further, we present the result of the PL measurements on the nanohybrid and controls, shown in Fig. 2(c). The VSe₂ are highly photoluminescent and show a broad peak centred at 455 nm. Strikingly, the PL intensity is drastically reduced and redshifted by 10 nm in the nanohybrid compared to VSe₂, indicating an efficient charge transfer. The charge transfer is enabled by the overlap of the SWCNT and VSe₂ electronic wave functions, which makes the potential barrier sufficiently small to facilitate charge transfer during photoexcitation. The mixing of electronic states at the interface changes the density of states, which will result in quenching and redshifting of the PL peak [50].

III. RESULTS AND DISCUSSION

Such nanoscopic charge-transfer interaction at the interfaces has been shown to dramatically alter the optoelectronic and chemical properties of the nanohybrid [51]. For instance, we recently reported an unprecedented enhancement in ultrafast third-order nonlinear optical response due to efficient direct charge transfer from Au shell to Sb₂Se₃ core when the metal is selectively excited at the plasmonic wavelength [52]. Thus, it is natural to ask, how does such nanoscopic charge transfer impact the ultrafast third-order nonlinear optical response in the SWCNT–VSe₂ nanohybrid. To measure the third-order nonlinear optical response, we employ open and closed aperture Z scan, which measures total transmittance as a function of incident laser intensity [53,54]. For the Z-scan measurements, samples are dispersed in distilled water, with a linear transmittance of approximately 70% at 800 nm.

Figure 3(a) shows the open-aperture Z-scan result of the nanohybrid and controls at 800 nm at a peak intensity of 111 GW cm⁻². At this moderate peak intensity, the Z-scan peak-shape response of the nanohybrid shows a very strong ESA, which is in sharp contrast to the SA of the control systems. The result of the Z-scan measurement at 560 nm at a peak intensity of 107 GW cm⁻² is shown in Fig. 3(b). In this case, also the Z-scan peak-shape response of the nanohybrid shows a very strong ESA, which is in contrast to the observed weak ESA of SWCNT and SA of VSe₂. The experimental data are fitted theoretically using the nonlinear absorption Eq. (S3) [23] (details in Sec. S4 within the Supplemental Material [39]),

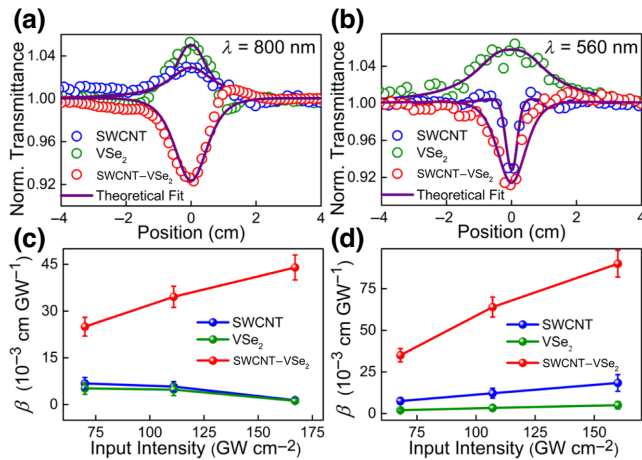


FIG. 3. Open-aperture Z-scan trace of SWCNT–VSe₂, SWCNT, and VSe₂. Normalized transmittance as a function of the position at excitation wavelength of (a) 800 nm, 111 GW cm⁻² (b) 560 nm, 107 GW cm⁻². Solid lines represent theoretical fit using Eq. S3 in Sec. S4 within the Supplemental Material [39]. Variation of β with excitation intensity at (c) 800 nm and (d) 560 nm.

and parameters from the best fit to the normalized transmittance data are shown in Table I. It can be seen from there that the ESA coefficient (β) value of the nanohybrid is found to be $\beta = (35 \pm 2) \times 10^{-2}$ cm GW⁻¹ at 800 nm. On the other hand, the β value of $(64 \pm 3) \times 10^{-2}$ cm GW⁻¹ for the nanohybrid at 560 nm is 5 times larger than the corresponding value for SWCNT. To further provide the experimental evidence on ESA, we perform intensity-dependent Z-scan measurements, which show that β and ESA cross section (σ_{ES}) has a monotonic increase with peak intensity [Figs. 3(c) and 3(d), and Table S2 within the Supplemental Material [39]]. This also supports the thesis of ultrafast charge transfer at the interface.

To establish the spectral range over which the nanohybrid shows ESA mediated via charge transfer, we repeat the experiment in the entire visible-to-near-infrared (400–900 nm) region. Strikingly, we find that the nanohybrid shows ESA in the entire region. However, in this

TABLE I. ESA coefficient (β) and saturation intensity (I_s), calculated by fitting the experimental data using Eq. (S3) within the Supplemental Material [39].

Excitation	Sample	β (10 ⁻³ cm GW ⁻¹)	I_s (10 ² GW cm ⁻²)
$\lambda = 800 \text{ nm}$	SWCNT	$-(6 \pm 0.2)$	6 ± 0.6
	VSe ₂	$-(5 \pm 0.3)$	10 ± 0.3
	SWCNT–VSe ₂	35 ± 2	2 ± 0.7
$\lambda = 560 \text{ nm}$	SWCNT	12 ± 1	7 ± 0.4
	VSe ₂	$-(3 \pm 0.7)$	20 ± 1
	SWCNT–VSe ₂	64 ± 3	4 ± 0.2

spectral region, VSe₂ shows only SA, whereas SWCNT displays either weak ESA or SA at the location of the van Hove singularities in the density of states. More details of other wavelength experimental data can be found in Sec. S5 within the Supplemental Material [39].

The contrasting SA and ESA response of the SWCNT can be understood in terms of its van Hove singularities [55]. The energy gaps between the van Hove singularities can be obtained using the zone-folding method [54], and it can be pictorially depicted using the well-known Kataura plot [56]. The excitation wavelengths 800 and 900 nm show that the SA is linked with the saturation of M_{11} and E_{22} transition (see Sec. S6 within the Supplemental Material [39]). These excitations guide a large population of carriers in the conduction band, which restricts further absorption of photons within the pulse duration due to Pauli blocking, giving rise to SA. On the other hand, the excitation wavelengths 400, 560, and 670 nm show weak ESA predominantly due to the transitions from E_{33} and E_{44} levels to the higher-energy levels [55]. Furthermore, VSe₂ exhibits SA at all excitation wavelengths except 400 nm, even when excited with photons of lower energy compared to the band gap. Such a result in VSe₂ is attributed to the band-structure modulation caused by V or Se atomic deformity [57] or the coexistence of metallic and semiconducting states in layered 2D materials [58]. Figure S14(c) within the Supplemental Material [39] shows the band structure of VSe₂, and the blue lines below the conduction band represent the sub-band-gap absorption band formed by the metallic state. Here, the saturation in absorption occurs as the conduction band is filled by the photoexcited carriers from the valence band.

We establish ESA, a third-order nonlinear optical process in SWCNT–VSe₂ over a broad spectral range, using charge transfer from donor VSe₂ to acceptor SWCNT. It is worthwhile to note that VSe₂ shows only SA (increased transparency at a high intensity) over the entire range, whereas SWCNT shows ESA at van Hove singularities and SA for other wavelengths. The condition for observing ESA is that the excited-state absorption cross section (σ_{ES}) must be greater than the ground-state absorption cross section (σ_{GS}), and if this condition is not satisfied, the material will show SA [7,59]. By charge transfer from donor to acceptor material, we can achieve the condition $\sigma_{\text{ES}} > \sigma_{\text{GS}}$. This way, we can induce ESA in materials that show only SA. For instance, SWCNT shows SA or weak ESA, which can be converted into ESA or enhanced to many orders by making a hybrid with electron-donating VSe₂. Table II shows that $\sigma_{\text{ES}} > \sigma_{\text{GS}}$ for SWCNT–VSe₂ due to charge transfer. These results certainly ascertain that the enhancement of the nonlinear optical properties of the nanohybrid is due to the charge transfer.

To understand the charge-transfer mechanism, we performed first-principles density-functional theory (DFT) calculations using the Vienna *ab initio* simulation package

TABLE II. Ground-state (σ_{GS}) and excited-state (σ_{ES}) absorption cross sections at 800 and 560 nm.

Excitation	Sample	σ_{GS} (10^{-20} cm^2)	σ_{ES} (10^{-20} cm^2)
$\lambda = 800 \text{ nm}$	SWCNT	1.8 ± 0.2	0.7 ± 0.1
	VSe ₂	2.0 ± 0.5	1.1 ± 0.2
	SWCNT–VSe ₂	1.3 ± 0.2	6.6 ± 0.8
$\lambda = 560 \text{ nm}$	SWCNT	0.5 ± 0.1	1.5 ± 0.2
	VSe ₂	1.0 ± 0.2	$0.3 \pm 10.$
	SWCNT–VSe ₂	1.5 ± 0.3	7.5 ± 0.9

(VASP) [60–63]. The details of the calculations [64–66] are presented in Sec. S7 within the Supplemental Material [39]. After optimizing the bulk geometry of VSe₂ we made the (001) plane of VSe₂ as it has an intense peak in the XRD pattern. The geometry optimized structure of the (001) plane of VSe₂ is depicted in Fig. 4(a). Using the optimized surface of VSe₂, we generate the nanohybrid layer SWCNT–VSe₂ considering the SWCNT to have the chirality of (8, 0). Then we allow the nanohybrid structure to relax, and the minimum energy configuration is shown in Fig. 4(b). To find the orbital interactions and the charge-transfer mechanism, we compute the atom projected partial density of states (PDOS). Figures 4(c) and 4(d) display the PDOS for C 2p orbital and V 3d orbital for the nanohybrid as well as their controls. From Fig. 4(c), it can be seen that the appearance of two intense peaks (blue color) around -1 eV and close to -6 eV below the Fermi level for C 2p orbital for SWCNT–VSe₂ (lower panel) (green elliptical circle) compared to that of control SWCNT (upper panel) (red elliptical circle). The appearance of intense peaks below the Fermi level (green elliptical circle) qualitatively indicates charge gain by the C 2p orbital of SWCNT when it interacts with VSe₂. Similarly, in Fig. 4(d), we can see an intense peak at the Fermi level for V 3d orbital (black line, upper panel) (green elliptical circle) of VSe₂, which is reduced for the case of SWCNT–VSe₂ as indicated by reduced peak (green line at Fermi level, lower panel) (red elliptical circle). The reduction in electronic states in the valence band of V 3d orbital and enhancement for C 2p orbital in the nanohybrid signify charge transfer from V 3d orbital to C 2p orbital. In order to obtain a quantitative estimate of the charge transfer, we perform the Bader-charge analysis. As per Bader, charge partitioning [67] estimates a transfer of $0.446e$ charge from each formula unit of VSe₂ to SWCNT. This charge transfer is likely to play a role in changing the optical properties of the composite structure, which shows ESA over a broad optical range, opposed to the individual decoupled materials, which either show no ESA or show ESA at very specific frequencies.

To find the spatial distribution of the charge-density variation, we plot the charge-density difference, $\rho(\text{SWCNT–VSe}_2) - \rho(\text{VSe}_2)$ in Fig. 4(e) for an isovalue

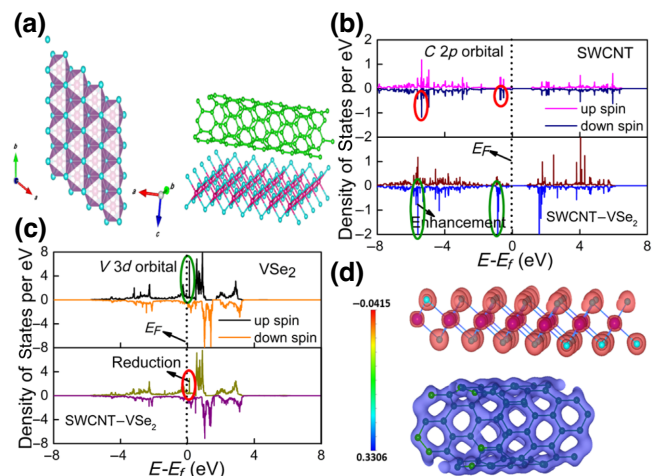


FIG. 4. (a) Geometry relaxed structure of the VSe₂ layer. (b) Optimized structure of the SWCNT–VSe₂ nanohybrid. Purple, cyan, and green spheres represent vanadium, selenium, and carbon atoms, respectively. (c) PDOS for the C 2p orbital of the control SWCNT (upper panel) and for SWCNT hybridized with VSe₂ (lower panel). The Fermi level is set at 0 eV, and it is denoted by a dotted line. There is an enhancement in electronic states (green elliptical circle) for the C 2p orbital of SWCNT when it is hybridized with VSe₂. (d) PDOS for the V 3d orbital of control VSe₂ (upper panel) and when VSe₂ is hybridized with SWCNT (lower panel). There is a reduction in electronic states (red elliptical circle) for the V 3d orbital of VSe₂ when it is hybridized with SWCNT. (e) Charge-density distribution plot for charge-density difference between SWCNT–VSe₂ and VSe₂ for isovalue of $0.107e$. The charge gain region in SWCNT is shown by blue color and charge-loss region in VSe₂ by red color.

of $0.107e$. The red region corresponds to the charge-loss region and the blue and green region corresponds to the charge-gain region. So, the charge density isosurfaces with red color over the VSe₂ region indicate charge loss from VSe₂, whereas charge-density isosurfaces in blue color over SWCNT indicate charge gain by SWCNT. Our PDOS analysis, Bader-charge analysis, and charge-density plot are consistent and indicate charge transfer from V 3d orbital to C 2p orbital, supporting the experimental findings. This equilibrium analysis indicates the possibility of charge transfer from VSe₂ to SWCNT in the nonequilibrium femtosecond regime. To model the Z-scan measurements, we adopt a minimal five-level rate equation, whose phenomenology is depicted in Fig. 5(a). Our model includes (i) one prominent optical transition in VSe₂, (ii) two prominent optical transitions in SWCNT (one from the ground state, and the other transition captures all excited state transitions between the multiple van Hove singularities of the SWCNT) and (iii) charge transfer from the photoexcited state in VSe₂ to the excited state in SWCNT. The five-level rate equation (see Sec. S8 within the Supplemental Material [39]) captures the time dynamics of the population $[N_{V1}, N_{V2}, N_{S1}, N_{S2}, N_{S3}]$ as indicated

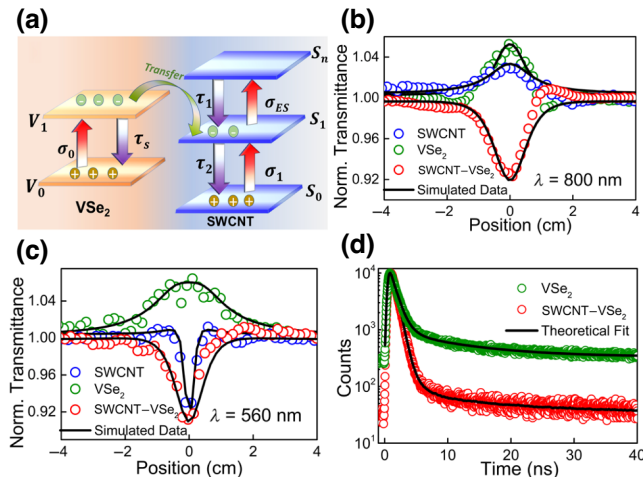


FIG. 5. (a) Schematic diagram of the charge-transfer mechanism through donor-acceptor interaction in a five-level model. Numerically simulated normalized transmitted intensity as a function of position using our five-level rate-equation model, which is in good agreement with the experimental results at (b) 800 nm and (c) 560 nm. (d) The decay lifetime of control VSe₂ and the nanohybrid as measured by time-resolved PL measurements.

in Fig. 5(a)] of each of these levels. Based on the dynamical population of these levels, the transmitted intensity through the sample can be obtained from,

$$\frac{dI(Z)}{dZ} = [-\sigma_0 N_{V0} - \sigma_1 N_{S0} - \sigma_{ES} N_{S1}] I(Z). \quad (1)$$

Here, $I(Z)$ is incident laser intensity, σ_0 is the ground-state absorption cross-section of VSe₂, σ_1 and σ_{ES} are the ground and excited state absorption cross-section of SWCNT, respectively.

The numerically simulated normalized transmitted intensity through the sample, using this five-level rate equation, broadly captures all the major features of the experimental measurements shown in Figs. 5(b) and 5(c), as indicated by the solid line. Upon photoexcitation, electrons from the valence band of VSe₂ are transferred to S_1 of SWCNT, and intraband absorption from the S_1 to the S_n state results in ESA. This can be inferred from the dramatic increase in σ_{ES} due to ultrafast charge transfer between VSe₂ and SWCNT.

To understand this better, we examine the time-resolved PL measurements upon excitation with a 298-nm laser and emission at 455 nm for control VSe₂ and nanohybrid, shown in Fig. 5(d). The experimental details are provided in Sec. S9 within the Supplemental Material [39]. The decay curves for the nanohybrid and control VSe₂ are nicely fitted by exponential functions, and the details of the fitting parameters are mentioned in Table S11 within the Supplemental Material [39]. We estimate the average

lifetime of the carriers using the following equation:

$$\langle \tau \rangle = \frac{\sum_{i=1}^3 A_i \tau_i}{\sum_{i=1}^3 A_i}. \quad (2)$$

Here, A_i and τ_i are the pre-exponential factors and excited-state fluorescence lifetimes associated with the i th component, respectively. The PL average lifetime of the VSe₂ is found to be (742 ± 60) ps, which drastically reduces to (238 ± 24) ps in SWCNT-VSe₂, indicating efficient charge transfer. Having demonstrated the idea of charge-transfer-mediated nonlinear absorption, we now focus on the sign and magnitude of the nonlinear refractive index (n_2). To investigate the n_2 , we employ closed aperture Z-scan measurement by putting a small aperture in the far field in front of the detector so that transmission reduces to one by third of the incident intensity, which results in the broadening or narrowing of the transmitted beam. Figures 6(a)–6(d) show the closed aperture Z-scan peak shape of the nanohybrid and control systems at 800 (560) nm wavelength at a peak intensity of 111 (107) GW cm⁻². The closed aperture Z-scan peak shapes demonstrate a prefocal transmittance minimum (i.e., the valley) followed by a postfocal transmittance maximum (i.e., the peak) pattern in the measured intensity range, which indicates a self-focusing nature (positive refractive nonlinearity) with $n_2 = (52 \pm 4) \times 10^{-6}$ and $(15 \pm 3) \times 10^{-7}$ cm² GW⁻¹ for nanohybrid, at 800 and 560 nm, respectively. Further, we explain the reason behind the mechanism of nonlinear refraction in nanohybrid and controls. The laser excitation with nonresonant wavelength generates the free carriers, which leads to the nonlinear refraction of a self-focusing nature of VSe₂. Meanwhile, the delocalized π electrons and free carrier in the conduction band of sp^2 domains may contribute to the nonlinear refraction of the self-focusing nature of SWCNT, and nanohybrid [68]. The estimated n_2 values using Eq. S4 [69] within the Supplemental Material [39] are presented in Table III. We find that the n_2 values of the nanohybrid are an order of magnitude higher than the controls.

The many-fold enhancement in the ESA and the nonlinear refractive index of nanohybrid over a broad spectral range indicates its potential application as an ideal optical limiter in the entire visible-to-near-infrared region. To

TABLE III. Nonlinear refractive index (n_2) is calculated by fitting the experimental data using Eq. S4 within the Supplemental Material [39].

Sample	$n_2 (10^{-6} \text{ cm}^2 \text{ GW}^{-1})$	$n_2 (10^{-7} \text{ cm}^2 \text{ GW}^{-1})$
	800 nm	560 nm
SWCNT	5.0 ± 0.2	1.3 ± 0.1
VSe ₂	4.2 ± 0.3	2.4 ± 0.3
SWCNT-VSe ₂	52 ± 4	15 ± 3

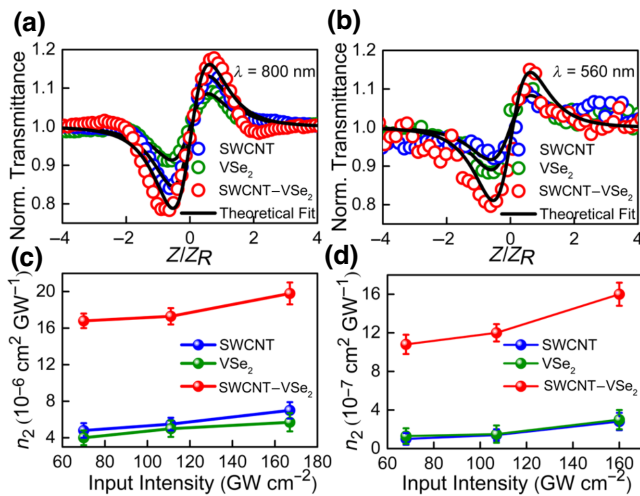


FIG. 6. Closed aperture Z-scan trace of SWCNT–VSe₂, SWCNT, and VSe₂. Normalized transmittance as a function of position at the excitation wavelength of (a) 800 nm, peak intensity of 111 GW cm^{-2} (b) 560 nm, peak intensity of 107 GW cm^{-2} . Solid lines represent the theoretical fit using Eq. S4 in Sec. S4 within the Supplemental Material [39]. The variation of n_2 with intensity at (c) 800 nm, (d) 560 nm.

demonstrate this, we construct a liquid cell-based optical limiter of path length 1 mm using the aqueous solution of SWCNT–VSe₂ as an optical-limiting medium. The schematic of our device is shown in Fig. 7(a), and it has a linear transmittance (T) of 70%. We characterize the strength of optical limiting of our device using the (i) onset threshold F_{on} defined as the input intensity at which the normalized transmittance starts to deviate from linearity and (ii) the limiting differential transmittance T'_{diff} ($= dI_{\text{out}}/dI_{\text{in}}$). An ideal optical limiter should have a very low F_{on} and low T'_{diff} . The onset threshold and differential transmittance measurement are shown in Sec. S10 within the Supplemental Material [39], and values are listed in Table IV. Figures 7(b) and 7(c) show F_{on} and T'_{diff} of

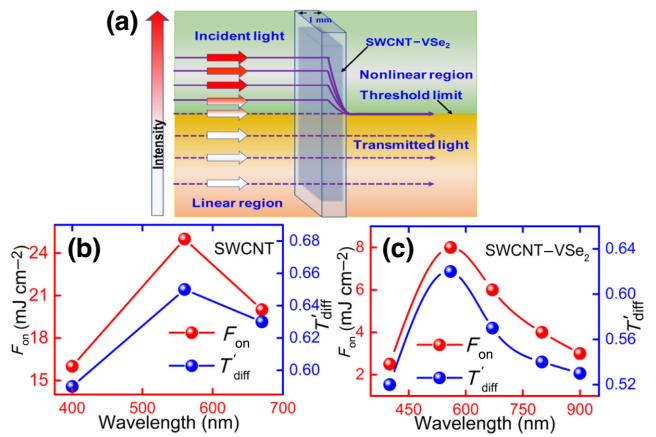


FIG. 7. (a) Schematic of the liquid cell-based optical-limiting device. It comprises a 1-mm path-length liquid cell that contains an aqueous solution of SWCNT–VSe₂ acting as an optical limiting medium. The concentration of the limiting medium in the distilled water is 1 mg/ml, with linear transmittance $T \approx 70\%$. When the lower intensity beams fall in the linear response regime (marked by yellow/red), our device will allow the light to pass through. However, above the threshold limit (green region), the system will act as an optical limiter and attenuate the intense beam. The threshold for the onset of nonlinearity F_{on} and the differential transmittance (T'_{diff}) of our device, as a function of the excitation wavelength for (b) SWCNT (c) SWCNT–VSe₂ nanohybrid.

our device as a function of the excitation wavelength in the entire visible-to-near-infrared region for SWCNT and SWCNT–VSe₂ nanohybrid, respectively. In the case of control VSe₂, this plot is not appreciable because, the near-infrared region, VSe₂ does not show optical limiting properties as they show SA. Our device sets a performance benchmark for optical limiting in the femtosecond regime over a wide spectral range. A comparison of our device's performance with other optical limiters in their respective wavelength range is presented in Table IV. An added advantage of our liquid-based optical limiters is that they

TABLE IV. Comparison of nonlinear optical parameters such as F_{on} and T'_{diff} of different optical limiters in visible-to-near-infrared region.

System	Wavelength (nm)	Lin T	F_{on} (mJ cm $^{-2}$)	T'_{diff}	References
SWCNT–VSe ₂	400	67	2.5	0.52	Present work
SWCNT–VSe ₂	560	70	8	0.62	Present work
SWCNT–VSe ₂	670	68	6	0.57	Present work
SWCNT–VSe ₂	800	70	4	0.54	Present work
SWCNT–VSe ₂	900	66	3	0.53	Present work
Au NP-RGO	532	70	50	0.3	[23]
ReS ₂	1064	90	700	0.64	[70]
Graphene thin film	532	73	10	0.1	[71]
Graphene nanoribbon	532	70	100	...	[72]
CdS nanoparticles	532	70	300	0.56	[73]
SiO ₂ -Se	800	85	54	...	[74]

self-heal, permitting high dynamic ranges limited only by the damage to cell windows.

IV. CONCLUSION

In summary, we demonstrate the ultrafast third-order nonlinear optical response of SWCNT–VSe₂ nanohybrid using the Z-scan technique with femtosecond laser pulses over the entire visible-to-near-infrared region due to synergistic charge transfer. Such donor-acceptor charge transfer in nanohybrid results in an unprecedented enhancement in the ESA and many-fold enhancement in the nonlinear refraction of self-focusing nature. Our first-principles-based calculations using the density-functional theory and Bader-charge analysis show electrons are transferred from VSe₂ to SWCNT. Based on this, we design a five-level rate-equation model that captures the physics of the ultrafast nonlinear optical response both qualitatively and quantitatively. Furthermore, we fabricate an optical-limiting device operating over the entire visible-to-near-infrared region with useful device parameters better than that found in several other benchmark optical limiters in the femtosecond regime. Our experimental and theoretical results in the nanohybrid provide alternative design guidelines for tuning and controlling the ultrafast third-order nonlinear optical response for potential applications in all-optical signal processing, optical switching, optical limiting for laser safety glasses, and quantum information with a wide operating bandwidth.

ACKNOWLEDGMENTS

The authors gratefully acknowledge the Science and Engineering Research Board (Projects No. EMR/2016/002520 and No. CRG/2019/002808), DAE BRNS [Sanction No. 37(3)/14/26/2016-BRNS/37245], and FIST Project for Department of Physics. B.C. acknowledges Dr Nandini Garg, Dr T. Sakutnala, Dr S.M. Yusuf, and Dr A.K. Mohanty for support and encouragement. The work at IIT Kanpur is supported by generous grants from Science and Engineering Research Board (SERB) and the Department of Science and Technology (DST) of the government of India.

- [1] R. W. Boyd *Nonlinear Optics* (Academic Press, Amsterdam Boston, 2008), 3rd ed.
- [2] W. L. Barnes, A. Dereux, and T. W. Ebbesen, Surface plasmon subwavelength optics, *Nature* **424**, 824 (2003).
- [3] M. R. Shcherbakov, P. Vabishchevich, A. Shorokhov, K. E. Chong, D. Y. Choi, I. Staude, A. E. Miroshnichenko, D. N. Neshev, A. A. Fedyanin, and Y. S. Kivshar, Ultrafast all-optical switching with magnetic resonances in nonlinear dielectric nanostructures, *Nano Lett.* **15**, 6985 (2015).

- [4] C. Farrera, F. Torres Andón, and N. Feliu, Carbon nanotubes as optical sensors in biomedicine, *ACS Nano* **11**, 10637 (2017).
- [5] J. D. Cox, I. Silveiro, and F. J. García De Abajo, Quantum effects in the nonlinear response of graphene plasmons, *ACS Nano* **10**, 1995 (2016).
- [6] J. H. Vella, J. H. Goldsmith, A. T. Browning, N. I. Limberopoulos, I. Vitebskiy, E. Makri, and T. Kottos, Experimental Realization of a Reflective Optical Limiter, *Phys. Rev. Appl.* **5**, 064010 (2016).
- [7] R. K. Yadav, J. Aneesh, R. Sharma, P. Abhiramnath, T. K. Maji, G. J. Omar, A. K. Mishra, D. Karmakar, and K. V. Adarsh, Designing Hybrids of Graphene Oxide and Gold Nanoparticles for Nonlinear Optical Response, *Phys. Rev. Appl.* **9**, 044043 (2018).
- [8] A. Marini, J. D. Cox, and F. J. García De Abajo, Theory of graphene saturable absorption, *Phys. Rev. B* **95**, 125408 (2017).
- [9] U. P. Generation, T. Hasan, Z. Sun, P. Tan, D. Popa, E. Flahaut, E. J. R. Kelleher, F. Bonaccorso, F. Wang, Z. Jiang, F. Torrisi, G. Privitera, V. Nicolosi, and A. C. Ferrari, Double-wall carbon nanotubes for wide-band, ultrafast pulse generation, *ACS Nano* **8**, 4836 (2014).
- [10] Y. Gladush, A. A. Mkrtchyan, D. S. Kopylova, A. Ivanenko, B. Nyushkov, S. Koltsev, A. Kokhanovskiy, A. Khegai, M. Melkumov, M. Burdanova, M. Staniforth, J. Lloyd-Hughes, and A. G. Nasibulin, Ionic liquid gated carbon nanotube saturable absorber for switchable pulse generation, *Nano Lett.* **19**, 5836 (2019).
- [11] D. M. Di Paola, P. M. Walker, R. P. A. Emmanuel, A. V. Yulin, J. Ciers, Z. Zaidi, J. F. Carlin, N. Grandjean, I. Shelykh, M. S. Skolnick, R. Butté, and D. N. Krizhanovskii, Ultrafast-nonlinear ultraviolet pulse modulation in an AlInGaN polariton waveguide operating up to room temperature, *Nat. Commun.* **12**, 3504 (2021).
- [12] D. Ielmini, Threshold switching mechanism by high-field energy gain in the hopping transport of chalcogenide glasses, *Phys. Rev. B* **78**, 035308 (2008).
- [13] D. Mandal, R. K. Yadav, A. Mondal, S. K. Bera, J. R. Aswin, P. Nemec, T. Halenovic, and K. V. Adarsh, Intensity mediated change in the sign of ultrafast third-order nonlinear optical response in As₂S₂ thin films, *Opt. Lett.* **43**, 4787 (2018).
- [14] K. P. Loh, Q. Bao, G. Eda, and M. Chhowalla, Graphene oxide as a chemically tunable platform for optical applications, *Nat. Chem.* **2**, 1015 (2010).
- [15] P. J. C. G. Henriques, H. C. Kamban, T. G. Pedersen, and N. M. R. Peres, Calculation of the nonlinear response functions of intraexciton transitions in two-dimensional transition metal dichalcogenides, *Phys. Rev. B* **103**, 235412 (2021).
- [16] S. Zhang, N. Dong, N. McEvoy, M. O'Brien, S. Winters, N. C. Berner, C. Yim, Y. Li, X. Zhang, Z. Chen, L. Zhang, G. S. Duesberg, and J. Wang, Direct observation of degenerate two-photon absorption and its saturation in WS₂ and MoS₂ monolayer and few-layer films, *ACS Nano* **9**, 7142 (2015).
- [17] Y. Murakami, E. Einarsson, T. Edamura, and S. Maruyama, Polarization Dependence of the Optical Absorption of Single-Walled Carbon Nanotubes, *Phys. Rev. Lett.* **94**, 087402 (2005).

- [18] H. Pan, Y. Feng, and J. Lin, Ab initio study of electronic and optical properties of multiwall carbon nanotube structures made up of a single rolled-up graphite sheet, *Phys. Rev. B* **72**, 085415 (2005).
- [19] C. Gu, H. Zhang, P. You, Q. Zhang, G. Luo, Q. Shen, Z. Wang, and J. Hu, Giant and multistage nonlinear optical response in porphyrin-based surface-supported metal-organic framework nanofilms, *Nano Lett.* **19**, 9095 (2019).
- [20] H. Baida, D. Mongin, D. Christofilos, G. Bachelier, A. Crut, P. Maioli, N. Del Fatti, and F. Vallée, Ultrafast Nonlinear Optical Response of a Single Gold Nanorod near Its Surface Plasmon Resonance, *Phys. Rev. Lett.* **107**, 057402 (2011).
- [21] I. V. Ryzhov, R. F. Malikov, A. V. Malyshev, and V. A. Malyshev, Nonlinear optical response of a two-dimensional quantum-dot supercrystal: Emerging multistability, periodic and aperiodic self-oscillations, chaos, and transient chaos, *Phys. Rev. A* **100**, 033820 (2019).
- [22] M. Consales, A. Ricciardi, A. Crescitelli, E. Esposito, A. Cutolo, and A. Cusano, Lab-on-fiber technology: Toward multifunctional optical nanoprobes, *ACS Nano* **6**, 3163 (2012).
- [23] R. Sharma, J. Aneesh, R. K. Yadav, S. Sanda, A. R. Barik, A. K. Mishra, T. K. Maji, D. Karmakar, and K. V. Adarsh, Strong interlayer coupling mediated giant two-photon absorption in MoSe₂/graphene oxide heterostructure quenching of exciton bands, *Phys. Rev. B* **93**, 155433 (2016).
- [24] S. Biswas, A. K. Kole, C. S. Tiwary, and P. Kumbhakar, Enhanced nonlinear optical properties of graphene oxide-silver nanocomposites measured by Z-scan technique, *RSC Adv.* **6**, 10319 (2016).
- [25] M. He, C. Quan, C. He, Y. Huang, L. Zhu, Z. Yao, S. Zhang, J. Bai, and X. Xu, Enhanced nonlinear saturable absorption of MoS₂/graphene nanocomposite films, *J. Phys. Chem. C* **121**, 27147 (2017).
- [26] V. Mamidala, G. Xing, and W. Ji, Surface plasmon enhanced third-order nonlinear optical effects in Ag-Fe₃O₄ nanocomposites, *J. Phys. Chem. C* **114**, 22466 (2010).
- [27] C. Quan, C. Lu, C. He, X. Xu, Y. Huang, Q. Zhao, and X. Xu, Band alignment of MoTe₂/MoS₂ nanocomposite films for enhanced nonlinear optical performance, *Adv. Mater. Interfaces* **6**, 21 (2019).
- [28] R. Zhang, J. Fan, X. Zhang, H. Yu, H. Zhang, Y. Mai, T. Xu, J. Wang, and H. J. Snaith, Nonlinear optical response of organic-inorganic halide perovskites, *ACS Photonics* **3**, 371 (2016).
- [29] P. Chen, W. W. Pai, Y. H. Chan, V. Madhavan, M. Y. Chou, S. K. Mo, A. V. Fedorov, and T. C. Chiang, Unique Gap Structure and Symmetry of the Charge Density Wave in Single-Layer VSe₂, *Phys. Rev. Lett.* **121**, 196402 (2018).
- [30] M. Chhowalla, H. S. Shin, G. Eda, L. J. Li, K. P. Loh, and H. Zhang, The chemistry of two-dimensional layered transition metal dichalcogenide nanosheets, *Nat. Chem.* **5**, 263 (2013).
- [31] Santu K. Bera, M. Shrivastava, K. Bramhachari, H. Zhang, A. K. Poonia, D. Mandal, E. M. Miller, M. C. Beard, Amit Agarwal, and K. V. Adarsh, Atomlike interaction and optically tunable giant band-gap renormalization in large-area atomically thin MoS₂, *Phys. Rev. B* **104**, L201404 (2021).
- [32] S. Iijima, Helical microtubules of graphitic carbon, *Nature* **354**, 56 (1991).
- [33] S. Ghosh, A. K. Sood, and N. Kumar, Carbon nanotube flow sensors, *Science* **299**, 1042 (2003).
- [34] F. Li, K. Tu, and Z. Chen, Versatile electronic properties of VSe₂ bulk, few-layers, monolayer, nanoribbons, and nanotubes: A computational exploration, *J. Phys. Chem. C* **118**, 21264 (2014).
- [35] B. E. Conway, Two-dimensional and quasi-two-dimensional isotherms for Li intercalation and UPD processes at surfaces, *Electrochim. Acta* **38**, 1249 (1993).
- [36] K. Xu, P. Chen, X. Li, C. Wu, Y. Guo, J. Zhao, X. Wu, Y. Xie, K. Xu, P. Z. Chen, C. Z. Wu, Y. Q. Guo, J. Y. Zhao, X. J. Wu, Y. Xie, and X. L. Li, Ultrathin nanosheets of vanadium diselenide: A metallic two-dimensional material with ferromagnetic charge-density-wave behavior, *Angew. Chem. Int. Ed.* **52**, 10477 (2013).
- [37] P. Kim, T. W. Odom, J. L. Huang, and C. M. Lieber, Electronic Density of States of Atomically Resolved Single-Walled Carbon Nanotubes: Van Hove Singularities and End States, *Phys. Rev. Lett.* **82**, 1225 (1999).
- [38] X. Zhang, A. Selkirk, S. Zhang, J. Huang, Y. Li, Y. Xie, N. Dong, Y. Cui, L. Zhang, W. J. Blau, and J. Wang, MoS₂/carbon nanotube core-shell nanocomposites for enhanced nonlinear optical performance, *Chem.: A Eur. J.* **23**, 3321 (2017).
- [39] See Supplemental Material at <http://link.aps.org/supplemental/10.1103/PhysRevApplied.19.044081> for the details on synthesis, PXRD analysis, Z-scan theory, five-level rate equation, computational details, fitting parameters, and optical limiting performance parameter measurement.
- [40] Sree RaJ KA, A. S. Shahajan, B. Chakraborty, and C. S. Rout, The role of carbon nanotubes in enhanced charge storage performance of VSe₂: Experimental and theoretical insight from DFT simulations, *RSC Adv.* **10**, 31712 (2020).
- [41] R. Y. N. Gengler, D. S. Badali, D. Zhang, K. Dimos, K. Spyrou, D. Gournis, and R. J. D. Miller, Revealing the ultrafast process behind the photoreduction of graphene oxide, *Nat. Commun.* **4**, 2560 (2013).
- [42] K. N. Kudin, B. Ozbas, H. C. Schniepp, R. K. Prud'Homme, I. A. Aksay, and R. Car, Raman spectra of graphite oxide and functionalized graphene sheets, *Nano Lett.* **8**, 36 (2008).
- [43] P. B. Amama, M. R. Maschmann, T. S. Fisher, and T. D. Sands, Dendrimer-templated Fe nanoparticles for the growth of single-wall carbon nanotubes by plasma-enhanced CVD, *J. Phys. Chem. B* **110**, 10636 (2006).
- [44] C. Fantini, A. Jorio, M. Souza, M. S. Strano, M. S. Dresselhaus, and M. A. Pimenta, Optical Transition Energies for Carbon Nanotubes from Resonant Raman Spectroscopy: Environment and Temperature Effects, *Phys. Rev. Lett.* **93**, 147406 (2004).
- [45] A. G. Souza Filho, S. G. Chou, G. G. Samsonidze, G. Dresselhaus, M. S. Dresselhaus, L. An, J. Liu, A. K. Swan, M. S. Ünlü, B. B. Goldberg, A. Jorio, A. Grüneis, and R. Saito,

- Stokes and anti-Stokes Raman spectra of small-diameter isolated carbon nanotubes, *Phys. Rev. B* **69**, 115428 (2004).
- [46] J. Pandey and A. Soni, Electron-phonon interactions and two-phonon modes associated with charge density wave in single crystalline 1T-VSe₂, *Phys. Rev. Res.* **2**, 033118 (2020).
- [47] S. Sugai and T. Ueda, High-pressure Raman spectroscopy in the layered materials 2H-MoS₂, 2H-MoSe₂, and 2H-MoTe₂, *Phys. Rev. B* **29**, 6554 (1982).
- [48] L. Liang and V. Meunier, First-principles Raman spectra of MoS₂, WS₂ and their heterostructures, *Nanoscale* **6**, 5394 (2014).
- [49] H. A. Zeinabad, A. Zarrabian, A. A. Saboury, A. M. O. Alizadeh, and M. Falahati, Interaction of single and multi-wall carbon nanotubes with the biological systems: Tau protein and PC12 cells as targets, *Sci. Rep.* **6**, 26508 (2016).
- [50] J. Yuan, S. Najmaei, Z. Zhang, J. Zhang, S. Lei, P. M. Ajayan, B. I. Yakobson, and J. Lou, Photoluminescence quenching and charge transfer in artificial heterostacks of monolayer transition metal dichalcogenides and few-layer black phosphorus, *ACS Nano* **9**, 555 (2015).
- [51] N. W. Ashcroft and N. D. Mermin, *Solid State Physics* (Harcourt College Publishers, Orlando, FL, 1976).
- [52] R. K. Yadav, J. Aneesh, R. Sharma, M. Salvi, J. Jayabalaji, H. Jain, and K. V. Adarsh, Giant enhancement of nonlinear absorption in graphene oxide—Sb₂Se₃ nanowire heterostructure, *J. Appl. Phys.* **125**, 025702 (2019).
- [53] M. Sheik-Bahae, A. A. Said, T. H. Wei, D. J. Hagan, and E. W. Van Stryland, Sensitive measurement of optical nonlinearities using a single beam, *IEEE J. Quantum Electron.* **26**, 760 (1990).
- [54] H. Li, S. Chen, D. W. Boukhvalov, Z. Yu, M. G. Humphrey, Z. Huang, and C. Zhang, Switching the nonlinear optical absorption of titanium carbide MXene by modulation of the surface terminations, *ACS Nano* **16**, 394 (2022).
- [55] B. Anand, R. Podila, P. Ayala, L. Oliveira, R. Philip, S. S. Sankara Sai, A. A. Zakhidov, and A. M. Rao, Nonlinear optical properties of boron doped single-walled carbon nanotubes, *Nanoscale* **5**, 7271 (2013).
- [56] H. Kataura, Y. Kumazawa, Y. Maniwa, I. Umezu, S. Suzuki, Y. Otsuka, and Y. Achiba, Optical properties of single-wall carbon nanotubes, *Synth. Met.* **103**, 2555 (1999).
- [57] S. Wang, H. Yu, H. Zhang, A. Wang, M. Zhao, Y. Chen, L. Mei, and J. Wang, Broadband few-layer MoS₂ saturable absorbers, *Adv. Mater.* **26**, 3538 (2014).
- [58] J. Zheng, H. Zhang, S. Dong, Y. Liu, C. Tai Nai, H. Suk Shin, H. Young Jeong, B. Liu, and K. Ping Loh, High yield exfoliation of two-dimensional chalcogenides using sodium naphthalenide, *Nat. Commun.* **5**, 2995 (2014).
- [59] R. L. Sutherland, *Handbook of Nonlinear Optics* (Dekker, New York, 2003), 2nd ed.
- [60] G. Kresse and J. Hafner, Ab initio molecular dynamics for liquid metals, *Phys. Rev. B* **47**, 558 (1993).
- [61] G. Kresse and J. Hafner, Ab initio molecular-dynamics simulation of the liquid-metal-amorphous-semiconductor transition in germanium, *Phys. Rev. B* **49**, 14251 (1994).
- [62] G. Kresse and J. Hafner, Efficiency of ab-initio total energy calculations for metals and semiconductors using a plane-wave basis set, *Comput. Mater. Sci.* **6**, 15 (1996).
- [63] G. Kresse and J. Furthmüller, Efficient iterative schemes for ab initio total-energy calculations using a plane-wave basis set, *Phys. Rev. B* **54**, 11169 (1996).
- [64] J. P. Perdew, K. Burke, and M. Ernzerhof, Generalized Gradient Approximation Made Simple, *Phys. Rev. Lett.* **77**, 3865 (1996).
- [65] H. J. Monkhorst and J. D. Pack, Special points for Brillouin-zone integrations, *Phys. Rev. B* **13**, 5188 (1976).
- [66] S. Grimme, Semiempirical GGA-type density functional constructed with a long-range dispersion correction, *J. Comput. Chem.* **27**, 1787 (2006).
- [67] W. Tang, E. Sanville, and G. Henkelman, A grid-based Bader analysis algorithm without lattice bias, *J. Phys. Condens. Matter* **21**, 084204 (2009).
- [68] X. L. Zhang, Z. B. Liu, X. C. Li, Q. Ma, X. Chen, J. Guo Tian, Y. Fei Xu, and Yong-Sheng Chen, Transient thermal effect, nonlinear refraction and nonlinear absorption properties of graphene oxide sheets in dispersion, *Opt. Express* **21**, 7511 (2013).
- [69] B. S. Kalanoor, L. Gouda, R. Gottesman, S. Tirosh, E. Haltzi, A. Zaban, and Y. R. Tischler, Third-order optical nonlinearities in organometallic methylammonium lead iodide perovskite thin films, *ACS Photonics* **3**, 361 (2016).
- [70] D. Mandal, M. Shrivastava, S. Sharma, A. K. Poonia, S. Marik, R. P. Singh, and K. V. Adarsh, Band edge carrier-induced sign reversal of an ultrafast nonlinear optical response in few-layer ReS₂ nanoflakes, *ACS Appl. Nano Mater.* **5**, 5479 (2022).
- [71] G. K. Lim, Z. L. Chen, J. Clark, R. G. S. Goh, W. H. Ng, H. W. Tan, R. H. Friend, P. K. H. Ho, and L. L. Chua, Giant broadband nonlinear optical absorption response in dispersed graphene single sheets, *Nat. Photonics* **5**, 554 (2011).
- [72] M. Feng, H. Zhan, and Y. Chen, Nonlinear optical and optical limiting properties of graphene families, *Appl. Phys. Lett.* **96**, 033107 (2010).
- [73] M. Feng, R. Sun, H. Zhan, and Y. Chen, Decoration of carbon nanotubes with CdS nanoparticles by polythiophene interlinking for optical limiting, *Carbon N. Y.* **48**, 1177 (2010).
- [74] K. A. Ann Mary, N. V. Unnikrishnan, and R. Philip, Cubic to amorphous transformation of Se in silica with improved ultrafast optical nonlinearity, *RSC Adv.* **5**, 14034 (2015).